CrossMark

RESEARCH PAPER

Highly efficient solid-state synthesis of carbon-encapsulated ultrafine MoO$_2$ nanocrystals as high rate lithium-ion battery anode

Boyang Liu · Yingfeng Shao · Yuliang Zhang · Fuhua Zhang · Ning Zhong · Wenge Li

Abstract A simple and highly efficient method is developed for the one-step in situ preparation of carbon-encapsulated MoO$_2$ nanocrystals (MoO$_2$@C) with core-shell structure for high-performance lithium-ion battery anode. The synthesis is depending on the solid-state reaction of cyclopentadienylmolybdenum tricarbonyl dimer with ammonium persulfate in an autoclave at 200 °C for 30 min. The large amount of heat generated during the explosive reaction cleaves the cyclopentadiene ligands into small carbon fragments, which form carbon shell after oxidative dehydrogenation coating on the MoO$_2$ nanocrystals, resulting in the formation of core-shell structure. The MoO$_2$ nanocrystals have an equiaxial morphology with an ultrafine diameter of 2–8 nm, and the median size is 4.9 nm. Hundreds of MoO$_2$ nanocrystals are encapsulated together by the worm-like carbon shell, which is amorphous and about 3–5 nm in thickness. The content of MoO$_2$ nanocrystals in the nanocomposite is about 69.3 wt.%. The MoO$_2$@C anode shows stable cyclability and retains a high reversible capacity of 443 mAh g^{-1} after 50 cycles at a current density of 3 A g^{-1}, owing to the effective protection of carbon shell.

B. Liu (✉) · Y. Zhang · F. Zhang · N. Zhong
College of Ocean Science and Engineering, Shanghai Maritime University, Shanghai 201306, China
e-mail: byliu@shmtu.edu.cn

Y. Zhang
e-mail: ylzhang@shmtu.edu.cn

F. Zhang
e-mail: fhzhang@shmtu.edu.cn

N. Zhong
e-mail: ningzhong@shmtu.edu.cn

Y. Shao (✉)
State Key Laboratory of Nonlinear Mechanics, Institute of Mechanics, Chinese Academy of Sciences, Beijing 100190, China
e-mail: shaoyf@lnm.imech.ac.cn

W. Li
Merchant Marine College, Shanghai Maritime University, Shanghai 201306, China
e-mail: wgli@shmtu.edu.cn

Introduction

Lithium-ion batteries (LIBs) have been universally accepted as power sources for different kinds of consumer electronics as well as electric/hybrid electric vehicles in terms of their high energy density, long cycle life, tiny memory effect, low toxicity, and cost (Jiang et al. 2014; Sasaki et al. 2013; Mancini et al. 2011). The performance of LIBs mainly depends on the intrinsic characteristics of electrode material, and the commercial graphite anode suffers from a low theoretical specific capacity of 372 mAh g^{-1} according to its fully lithiated stoichiometry of LiC$_6$ (Zhou et al. 2012; He et al. 2016). Consequently,

Springer

in the past decades, a lot of efforts have been made worldwide for exploring various candidates with different nanostructure and physicochemical property to improve the battery performance. Transition metal oxides typically demonstrate significantly higher theoretical specific capacities than graphite and have been intensively investigated as potential anodes in LIBs field (Ji et al. 2011). Among them, molybdenum dioxide (MoO_2) is one of the most attractive electroconductive metal oxides and exhibits a metallic type of conductivity with a small resistivity of 8.8×10^{-5} Ω cm at room temperature (Shi et al. 2009). Additionally, MoO_2 can deliver a high theoretical specific capacity of 838 mAh g^{-1} and possess a high electrochemical activity for the storage of lithium-ions (Zhang et al. 2014). Therefore, together with the affordable cost, MoO_2 is regarded as a very appealing anode candidate for high-performance LIBs. However, MoO_2 undergoes a large volume change during lithium-ion insertion/extraction process, and the kinetics associated with the lithium reduction of MoO_2 is sluggish because of the incomplete four-electron lithiation, resulting in serious capacity fading and poor cycling performance (Zhou et al. 2011).

To address the aforementioned issues, MoO_2 in nanocrystalline forms is widely used to reduce the diffusion path length for lithium-ions thereby improving both capacity and cyclability (Sun et al. 2011; Ku et al. 2009). Another common strategy involves incorporation of MoO_2 with carbonaceous materials, which can further enhance the electronic conductivity and buffer the volume expansion (Huang et al. 2014; Zhang and Yu 2015; Liu et al. 2013). Thus, MoO_2/carbon nanocomposite is considered as a promising high-performance anode material in LIBs, and several synthesis methods have been developed. The hydrothermal reaction is primarily used to fabricate MoO_2 nanoparticles in solution, in which ammonium heptamolybdate (($NH_4)_6Mo_7O_{24}$ $4H_2O$) (AHM) is almost the only one precursor for the evolution of MoO_2. For example, MoO_2 nanoparticles of 20–80 nm in diameter homogeneously anchored on graphene oxides (GO) were fabricated by keeping AHM in the GO suspension at 160–180 °C for 16–26 h, respectively (Bhaskar et al. 2012; Wang et al. 2015; Xu et al. 2012). MoO_2/graphene nanocomposite could be further obtained by the addition of reducing agent (citric acid) during the hydrothermal process or by

annealing treatment of MoO_2/GO at 600 °C under N_2 atmosphere. Similarly, carbon-coated uniform MoO_2 porous nanospheres of 60–80 nm were prepared by a hydrothermal treatment of AHM, ethylene glycol, and polyvinylpyrrolidone in an autoclave at 180 °C for 60 h followed by a subsequent anneal at 700 °C for 4 h in a flow of N_2 (Wang et al. 2010). It is evident that these multi-step synthesis processes always involve long time treatment and high-temperature annealing rather than the simultaneous in situ generation because of the different formation mechanisms of carbon and MoO_2 (Liu et al. 2012a, b). Otherwise, the carbon coating is prone to non-uniformity on the small MoO_2 nanoparticles, and the products usually have a broad size distribution and lacked regularity, leading to the unsatisfied rate capability and cycling performance. Consequently, it is still an ongoing issue to explore simple, efficient, high yield, and environmentally friendly preparation techniques by new formation mechanisms for overcoming the shortcomings of current methods.

In the present work, a novel solid-state reaction between cyclopentadienylmolybdenum tricarbonyl dimer (($C_5H_5)_2Mo_2(CO)_6$) and ammonium persulfate (($NH_4)_2S_2O_8$) has been developed for the one-step in situ preparation of carbon-encapsulated ultrafine MoO_2 nanocrystals (MoO_2@C) with core-shell structure. MoO_2@C with homogeneous morphology exhibits high specific capacity and rate capability, as well as excellent cycling stability.

Experimental

Materials and preparation

All the chemicals were received as analytical reagent grade and used without further purification. In detail, 5 mmol of ($C_5H_5)_2Mo_2(CO)_6$ ($Cp_2Mo_2(CO)_6$) and 20 mmol of ($NH_4)_2S_2O_8$ (APS) were weighed and manually milled by an agate mortar. Then, the homogeneously mixed reactants were sealed in an autoclave with a 200-ml polytetrafluoroethylene (PTFE) liner and held at 200 °C in an electric furnace for 30 min. After the reaction, the as-prepared powder was thoroughly rinsed with deionized water and ethanol in sequence to remove the soluble byproducts, and 1.1 g of MoO_2@C was eventually obtained after being dried in a vacuum oven at 60 °C.

Characterization

Phase structures of the sample were characterized by X-ray diffraction (XRD) using a PANalytical X'Pert PRO diffractometer with Cu K$_\alpha$ radiation. Raman spectrum of the carbon shell was recorded by a Bruker Senterra micro Raman spectrometer with an excitation wavelength of 633 nm at 2 mW. The surface morphology, microstructure, and composition of the sample were analyzed by field-emission scanning electron microscopy (SEM, JEOL JSM 7500F) and transmission electron microscopy (TEM, JEOL JEM 2010) equipped with an X-ray energy-dispersive spectroscopy system (EDS, EDAX). The reaction behaviors of the reactants and the final product in an ambient atmosphere were determined by differential scanning calorimetry and thermogravimetric analysis (DSC-TG, Netzsch STA 449F3) using open pans, respectively. The DSC of the reactants in a sealed aluminum pan was also carried out on a Netzsch DSC 204F1 to simulate the reactions in the autoclave. The Brunauer-Emmett-Teller (BET) surface area, Barrett-Joyner-Halenda (BJH), and density functional theory (DFT) pore size distribution of MoO$_2$@C were calculated from the adsorption branch of the nitrogen isotherms at 77 K on a Micromeritics ASAP 2020 porosimeter.

Electrochemical measurements

For the fabrication of working electrodes, MoO$_2$@C, acetylene black, and polyvinyl difluoride (PVDF) in a weight ratio of 80:10:10 were evenly mixed in N-methyl-2-pyrrolidone (NMP) solvent. The as-prepared slurry was coated on a thin copper foil (ϕ = 14 mm) and then thoroughly dried in vacuum at 120 °C. The electrochemical tests were conducted by the assembly of coin-type cell in an Ar-filled glove box with lithium foil as the counter electrode separated by a Celgard 2400 microporous polypropylene film. The 1.0 M LiPF$_6$ solution in a mixture of ethylene carbonate (EC) and dimethyl carbonate (DMC) (1:1 in volume) was used as the electrolyte. The galvanostatic charge/discharge curves of cells were measured on a battery testing system (Neware, BST-5V3mA) between 0.05 and 3 V versus Li/Li$^+$ at different current densities. The cyclic voltammogram (CV) was performed on a CHI 630A electrochemical workstation in the voltage range of 0.01–3.0 V and at a scan rate of 0.5 mV s^{-1}.
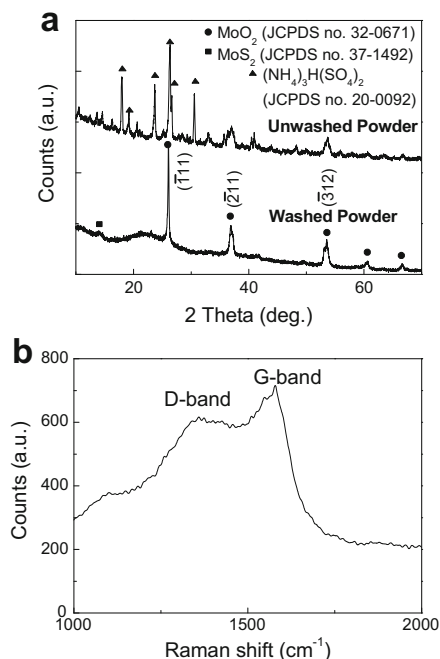

Fig. 1 **a** XRD patterns and **b** Raman shift of the MoO$_2$@C

Results and discussion

The XRD results in Fig. 1a indicate that all the strong diffraction peaks of the as-prepared black sample can be indexed to (NH$_4$)$_3$H(SO$_4$)$_2$, which is regarded as the main byproduct with good crystallinity ascribing to the decomposition of APS. After removal of (NH$_4$)$_3$H(SO$_4$)$_2$ through the washing process, the sharp peaks located at 2θ = 26°, 37°, and 53° can be unambiguously assigned to the strongest characteristic peaks of MoO$_2$ (−111), (−211), and (−312), respectively. It should be noted that the small peak at 2θ = 14° corresponds to the most intensive peak of MoS$_2$ (002). Since the peak of MoO$_2$ (−111) is much stronger than MoS$_2$ (002), MoO$_2$ are preferentially and abundantly formed by the oxidation of Cp$_2$Mo$_2$(CO)$_6$. On the other hand, carbon diffraction peaks are absent, and only a broad peak around 2θ = 22° can be found. However, the carbon shell can be clearly proved by the two typical D- and G-band Raman shifts located at 1360 and 1580 cm^{-1}, respectively, as shown in Fig. 1b. The relatively high-intensity D-band peak confirms that amorphous carbon with lattice distortion is obtained because the low synthesis temperature is not beneficial to the formation of graphitizable carbon. Notably, the as-prepared black powder in the
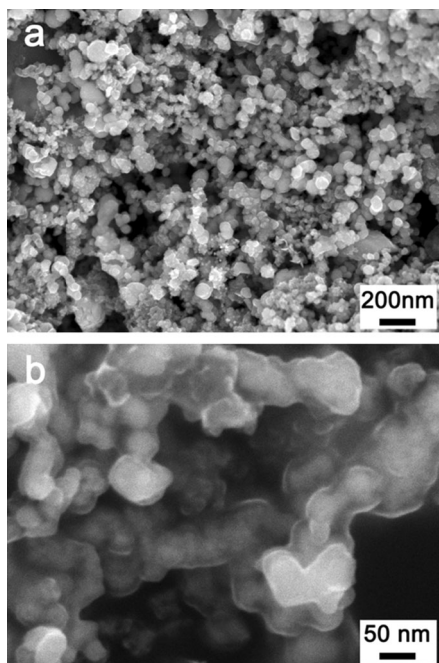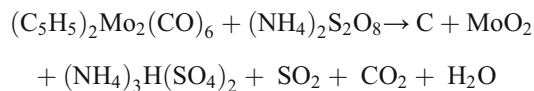
Fig. 2 SEM images of the MoO₂@C at different magnifications

products above, the major reaction formula in the process is proposed as follows:

$$(C_5H_5)_2Mo_2(CO)_6 + (NH_4)_2S_2O_8 \rightarrow C + MoO_2$$
$$+ (NH_4)_3H(SO_4)_2 + SO_2 + CO_2 + H_2O$$

The low magnification SEM image of the MoO₂@C in Fig. 2a reveals that the sample has a uniform morphology and consists of equiaxial nanoparticles, demonstrating that the solid-state synthesis is very simple and effective to yield a highly homogeneous product. It is distinct that the nanoparticles have a typical diameter less than 100 nm and aggregate together. At high magnification, these nanoparticles obviously show core-shell structure composed of white cores inside and an exterior semitransparent thin layer, corresponding to MoO₂ nanocrystals and carbon shell (Fig. 2b). Moreover, the carbon layer encapsulates lots of MoO₂ nanocrystals as a whole, rather than separately and individually encapsulates each nanocrystal.

The TEM images can provide further details on the morphology and microstructure of MoO₂@C. In Fig. 3a, it can be seen that the white inner cores under

autoclave emitted a pungent and irritating smell and adhered to some small liquid droplets, which should be SO_2 and H_2O. Consequently, according to these
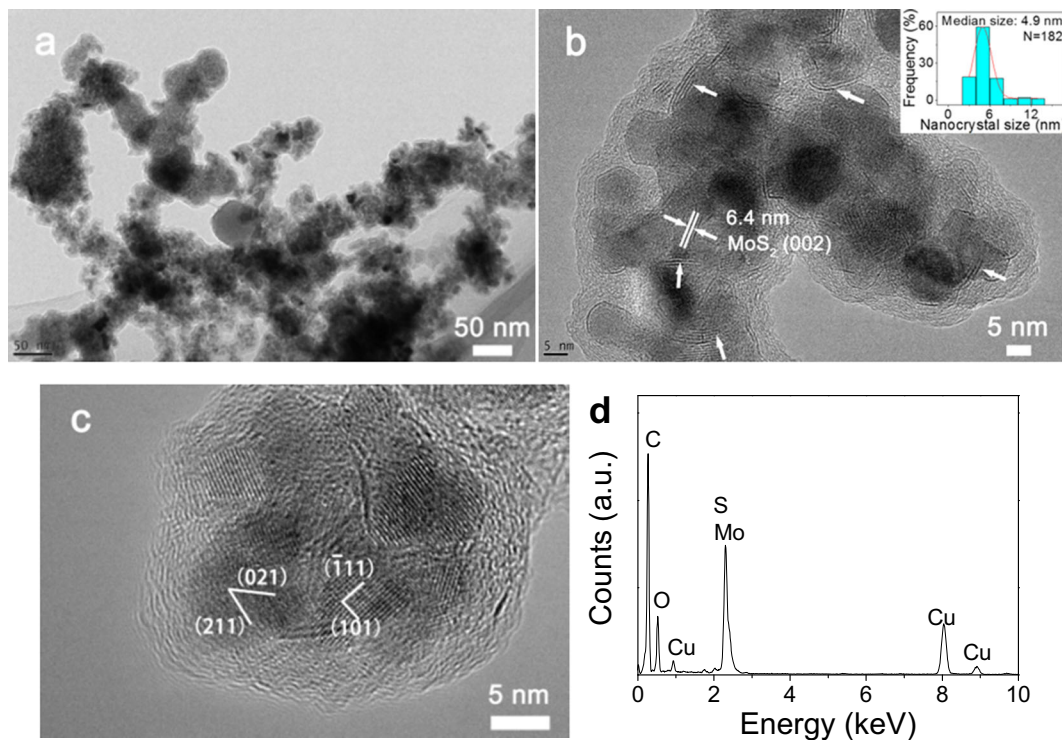

Fig. 3 a–c TEM, HRTEM images and d EDS spectrum of MoO₂@C, inset is the size distribution of MoO₂ nanocrystals

the carbon layer in SEM image are actually the agglomerated ultrafine nanocrystals. The worm-like carbon shell is interconnected and encapsulates hundreds of nanocrystals inside, exhibiting a uniform core-shell structure. These small nanocrystals also show an equiaxial morphology, and the carbon shell is about 3–5 nm in thickness (Fig. 3b). The nanocrystal size is accurately measured in several TEM images, and the nanocrystals have an ultrafine size of 2–8 nm according to the histogram (inset of Fig. 3b), where the median size is 4.9 nm. As a reference, the mean size of MoO_2 nanocrystals is also calculated by the Scherrer equation (Supplementary Material, Fig. S1 and Table S1), which is as small as 15.95 nm. Therefore, this method is more inclined to form ultrafine MoO_2 nanocrystals compared to the general hydrothermal route (Bhaskar et al. 2012; Wang et al. 2015; Xu et al. 2012; Wang et al. 2010). Besides the nanocrystals, a small amount of few-layered graphene-like structure indicated by the white arrows can also be observed and the interlayer space is about

0.64 nm, which is in agreement with the (002) crystalline plane of hexagonal MoS_2. It is illustrated that MoS_2 and MoO_2 are co-encapsulated by carbon, and MoO_2 is the dominant product. Additionally, graphene-like MoS_2 is also a popular anode material with high reversible capacity and rate capability (Chang et al. 2013; Huang et al. 2013; Yang et al. 2012), which can further enhance the electrochemical properties of the nanocomposite. Figure 3c shows that a two-dimensional lattice image of carbon encapsulated some typical equiaxial nanocrystals. The carbon shell is further proved to be amorphous according to its disordered lattice fringes. On the other hand, lattice fringes in the two nanocrystals can be well indexed to (021) and (211), (−111) and (101) planes of MoO_2, respectively. The EDS spectrum of the sample validates that C, Mo, O, and S are the main elements, while the Cu signal is from the copper grid (Fig. 3d). From tens of SEM and TEM images, it is found that all the MoO_2 nanocrystals are perfectly and homogeneously encapsulated by carbon. Although the
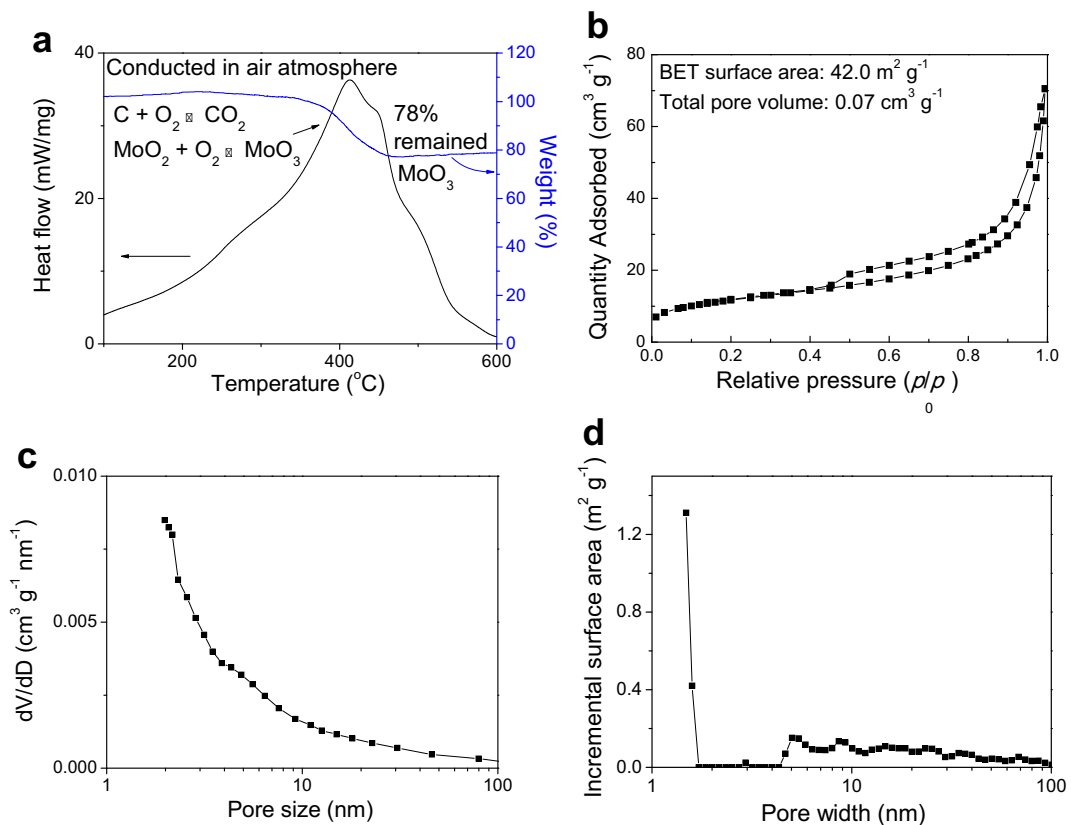

Fig. 4 a DSC-TG curve; b N_2 isotherms, BET surface area, and total pore volume; c BJH pore size distribution; and d DFT pore size distribution of the MoO_2@C

solid-phase-based synthesis is very simple, the morphology and quality of MoO_2@C can be effectively guaranteed.

The DSC-TG analysis conducted in air atmosphere is used to evaluate the composition of MoO_2@C. The weight loss around 400 °C in the TG curve is accompanied by a strong exothermic peak in the DSC curve, implying that the exterior carbon shell is burned off during this stage (Fig. 4a). At the same time, the inner MoO_2 cores are exposed to oxygen and subsequently oxidized to MoO_3. After 500 °C, the oxidation of MoO_2@C is completed, and the TG curve shows a steady plateau with a residue of 78.0% of the initial mass. Consequently, the content of MoO_2 nanocrystals is finally calculated to be 69.3 wt.% regardless of the MoS_2 impurity. The nitrogen isotherms, BET surface area, and total pore volume of the MoO_2@C are shown in Fig. 4b. The broad hysteresis loop in the relative pressure range of 0.4–1.0 is associated with the existence of mesopores, and the upward curvature at the relative pressure higher than 0.8 corresponds to the cylindrical mesopores (Janssen et al. 2003). However, the BET surface area and total pore volume of the MoO_2@C should be relatively small according to the low adsorbing capacity under the pressure of 0.97, which are calculated to be 42.0 m^2 g^{-1} and 0.07 cm^3 g^{-1}, respectively. Therefore, it is reasoned that carbon shell and MoO_2 cores are in close contact with each other. Furthermore, the isotherm indicates its mesoporosity with the type IV on the basis of the Brunauer, Deming, Deming, and Teller (BDDT) classification (Brunauer et al. 1940). The hysteresis loops of the adsorption/desorption isotherms seem to be a mixed type of H1 and H3 character that corresponds to cylindrical and slit-shaped pore geometries, respectively (Arachchige 2007). The BJH pore size distribution of the MoO_2@C in Fig. 4c shows that mesopores less than 30 nm are dominant in the sample. The DFT pore size distribution in Fig. 4d distinctly reveals micropores and mesopores in the range of 1–2 and 5–30 nm, respectively. The width of the pore size distribution curves is similar in both cases, demonstrating the presence of mesopores with wide size distribution in the MoO_2@C.

Figure 5a shows the DSC-TG curves of the pure APS and the mixture of $Cp_2Mo_2(CO)_6$ and APS in open alumina pans, respectively. It is obvious that the pure APS will exothermically decompose at about 190 °C to create oxygen (Erdey et al. 1964). When $Cp_2Mo_2(CO)_6$ is added, the reaction temperature is
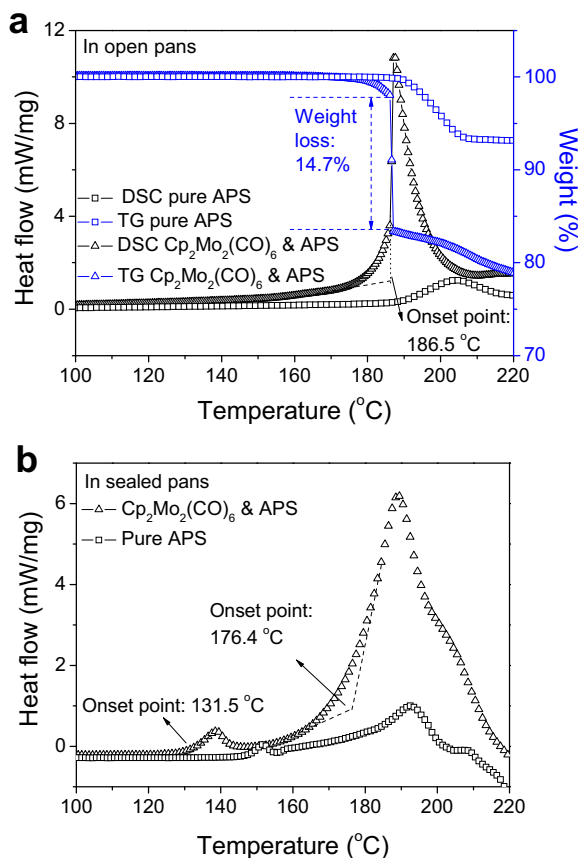

Fig. 5 a DSC-TG and b DSC of the reactants in open and sealed pans, respectively

distinctly reduced to 186.5 °C (onset point), and the mixture suffers a much stronger exothermic reaction than pure APS according to the intensive peak in the DSC curve. Meanwhile, the sample weight instantaneously loses 14.7% of the initial mass based on the TG curve, which should be caused by the release of generated gases. After that, the sample weight slowly decreases with the increment of temperature. These phenomena imply that an explosive reaction takes place between the two solid reactants and a large amount of heat and gases are generated. With the purpose of simulating the reaction behavior in the autoclave, the DSC analyses of the reactants in sealed aluminum pans are further carried out, as shown in Fig. 5b. A small new exothermic peak is revealed around 148.0 °C for pure APS, and it is probably due to the existence of a tiny moist air sealed in the pan, which can promote the decomposition of APS. The second peak around 190 °C is similar to that in the

open pan and slightly shifts to the low-temperature region. It can be explained that the decomposition products sealed in the reactor can further accelerate the reaction. When $Cp_2Mo_2(CO)_6$ is introduced, the initial peak at 131.5 °C is attributed to the decomposition of APS under the residual moist air and the subsequent oxidation of $Cp_2Mo_2(CO)_6$. Notably, the dominant peak at 176.4 °C becomes much broader and stronger, corresponding to the spontaneous ignition of $Cp_2Mo_2(CO)_6$ and liberation of H_2O, CO_2, and SO_2. It has been proved that the ammonium and oxidizing ions tend to reduce the stability of metallocene complexes and destroy the ferrocene-like sandwich structure at about 200 °C (Liu et al. 2007; Liu et al. 2014a, b; Liu et al. 2012b; Liu et al. 2015a, b). Compared to the reaction in the open pan, lots of heat and gases generated in the process are encapsulated in the sealed pan, quickly rising the temperature and pressure in the reactor. Therefore, the temperature in the autoclave will be much higher than 200 °C, and the cyclopentadiene ligands in $Cp_2Mo_2(CO)_6$ are cleaved into small carbon fragments, which eventually turn to carbon shell after oxidative dehydrogenation. In

addition, the Mo atoms and carbonyl groups in $Cp_2Mo_2(CO)_6$ will be oxidized to MoO_2 and CO_2, respectively. On the contrary, APS is reduced to SO_2 and $(NH_4)_3H(SO_4)_2$. It is also deduced that some APS can be transformed to sulfur by deep reduction (Liu et al. 2015a, b), which then combines with Mo to form a few of MoS_2. During the explosive reaction, carbon fragments filled the autoclave inhibit the grain growth of MoO_2, resulting in the formation of ultrafine MoO_2 nanocrystals. And the π interaction between Mo and carbon fragments should be responsible for the creation of core-shell structure (Liu et al. 2016).

Figure 6a displays the first three CV cycle profiles for MoO_2@C anode at a scan rate of 0.5 mV s^{-1} between 0.01–3 V. The wide irreversible peak located at around 0.9 V only appears in the first cycle and can be associated with the formation of solid electrolyte interphase (SEI) film on the carbon shell. In the subsequent cycles, the pronounced broad redox couple located at 1.2/1.5 V corresponds to the reversible phase transitions of partially lithiated Li_xMoO_2 during lithium insertion and extraction (Zhou et al. 2011; Sun et al. 2011; Liu et al. 2014b). Otherwise, due to the existence of MoS_2, the
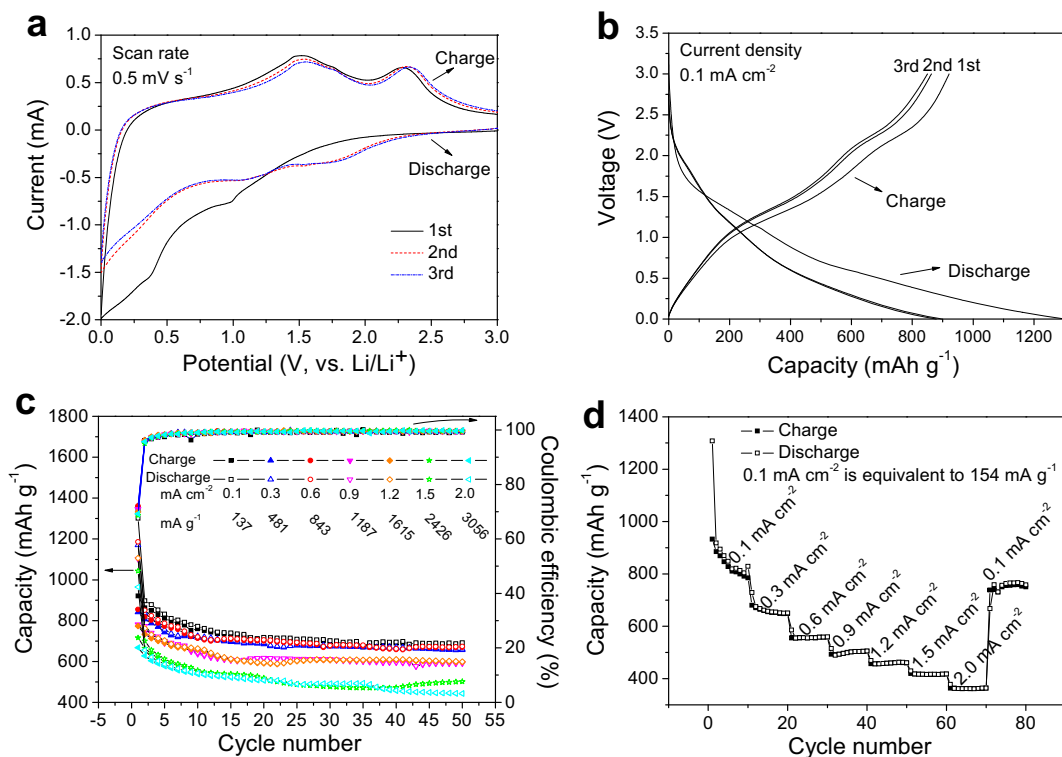

Fig. 6 Electrochemical performances of MoO_2@C anodes: **a** cyclic voltammograms at a scan rate of 0.5 mV S^{-1}, **b** the charge/discharge curves at a current density of 0.1 mA cm^{-2}, **c** cycling stability and Coulombic efficiency, **d** rate performance

redox peaks at 1.7 and 2.3 V can be ascribed to two-step Li-ion removal from Mo via reduction and oxidation of Li_2S into sulfur, respectively (Sen and Mitra 2013). The charge/discharge profiles in Fig. 6b demonstrate that the MoO_2@C anode possesses an initial discharge and charge capacity of 1301 and 921 mAh g^{-1}, respectively, corresponding to an irreversible capacity loss of 29% due to the SEI film formation. The charge plateaus at 1.5 and 2.3 V are in accordance with the CV curves.

The cycling stability and Coulombic efficiency of MoO_2@C anodes at various current densities are exhibited in Fig. 6c. The MoO_2@C anode shows good capacity retention during the 50 successive cycles at 0.1 mA cm^{-2} (137 mA g^{-1}) and still maintains a high reversible capacity of 687 mAh g^{-1}. When the current density is elevated, a high reversible capacity of 656, 670, 591, 597, 500, and 443 mAh g^{-1} after 50 cycles can be obtained at 0.3, 0.6, 0.9, 1.2, 1.5, and 2.0 mA cm^{-2} (about 3 A g^{-1}), respectively. MoO_2@C retains a higher capacity than the reported pure MoO_2 nanoparticles and most MoO_2/carbon composites at high rate, as summarized in Table 1, probably owing to the entire carbon encapsulation and the stable

core-shell structure. The Coulombic efficiencies rapidly increase to about 98% in the fifth cycle and are well maintained around 100% in the following cycles, illustrating the ultrafine MoO_2 nanocrystals enable the facile transport of lithium-ions and electrons in the nanocomposite. The rate capability of MoO_2@C is investigated by stepwise increasing the current density for every 10 cycles from 0.1 to 2.0 mA cm^{-2} and then returning back (Fig. 6d). The MoO_2@C anode shows outstanding high rate performance with a small decline in capacity as the current density increase. Remarkably, when the current density decreases from 2.0 to 0.1 mA cm^{-2}, the capacity of MoO_2@C anode returns from 364 to 668 mAh g^{-1} at once and further increases to a stable stage of 758 mAh g^{-1}, implying that the anode is highly stable and reversible.

In order to validate the effectiveness of carbon shell protection, the morphology of the MoO_2@C at the current density of 3 A g^{-1} after different cycles is studied by SEM, as shown in Fig. 7. After the first cycle, the surface of the MoO_2@C is smooth, and some tiny cracks can be observed (Fig. 7a).

Table 1 A state-of-the-art literature review of the capacity of pure MoO_2 and MoO_2@C composite in the voltage of 0–3 V

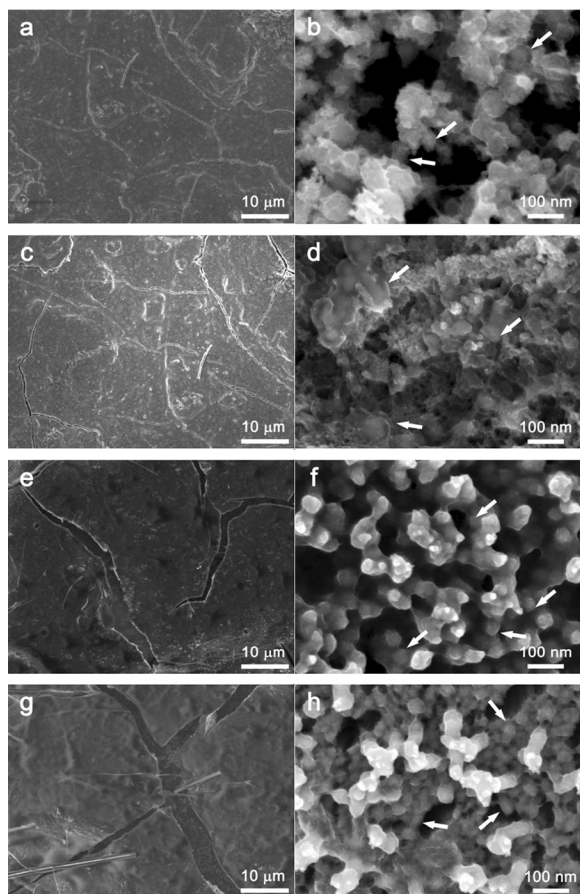| Materials	Current density (mA g^{-1})	Cycle number	Capacity (mAh g^{-1})	Ref.
MoO_2@C	137	50	687	This work
	481		656	
	1187		591	
	3056		443	
MoO_2@C	200	50	629	Zhou et al. 2011
	400		554	
Hierarchical MoO_2	200	20	719	Sun et al. 2011
MoO_2 particles			328	
MoO_2@Graphene	200	50	813	Huang et al. 2014
	1000	25	544	
MoO_2 particles	200	50	179	
	1000	25	115	
MoO_2 nanobelts@C	100	30	617	Yang et al. 2012
	500		412	
	1000		327	
MoO_2@C	200	50	821	Liu et al. 2013
	800	50	654	
MoO_2 particles	200	50	411	
MoO_2@Graphene	540	50	962	Bhaskar et al. 2012
	1042		497	
	2045		427	
MoO_2	200		215	

Fig. 7 SEM images of the MoO_2@C anodes after different cycles: **a**, **b** 1th, **c**, **d** 10th, **e**, **f** 50th, **g**, **h** 100th

Additionally, the width of some cracks becomes bigger with the increment of cycling number, which should be closely related to the MoO_2 volume change during lithium-ion insertion/extraction process (Fig. 7c–g). However, the MoO_2@C does not peel off from the current collector and is highly durable. At high magnification images, it is also remarkable that core-shell structure can be indicated by the white arrows, implying that the carbon shell is sufficiently stable to suppress volume expansion of MoO_2 (Fig. 7b–h).

Conclusion

A novel and efficient low-temperature solid-state reaction has been successfully developed for the one-step in situ preparation of MoO_2@C with core-shell structure. The rapid generation of a large amount of heat in the autoclave cleaves the cyclopentadiene ligands into small carbon fragments, which form carbon shell after oxidative dehydrogenation coating on the MoO_2 nanocrystals, resulting in the formation of core-shell structure. The median size of ultrafine equiaxial MoO_2 nanocrystals is 4.9 nm, and the thickness of amorphous carbon shell is 3–5 nm. MoO_2@C anode shows high capacity and stable cyclability at fast charge/discharge rate owing to the good protection of carbon shell.

References

Arachchige IU (2007) Sol–gel routes for metal chalcogenide nanoparticle assembly. Dissertation, Wayne State University

Bhaskar A, Deepa M, Rao TN et al (2012) Enhanced nanoscale conduction capability of a MoO_2/graphene composite for high-performance anodes in lithium ion batteries. J Power Sources 216:169–178. doi:10.1016/j.jpowsour.2012.05.050

Brunauer S, Deming LS, Deming WE, Teller E (1940) On a theory of the van der Waals adsorption of gases. J Am Chem Soc 62: 1723–1732. doi:10.1021/ja01864a025

Chang K, Geng D, Li X, Yang J, Tang Y, Cai M, Li R, Sun X (2013) Ultrathin MoS_2/nitrogen-doped graphene nanosheets with highly reversible lithium storage. Adv Energy Mater 3: 839–844. doi:10.1002/aenm.201201108

Erdey L, Gal S, Liptay G (1964) Thermoanalytical properties of analytical-grade reagents: ammonium salts. Talanta 11:913–940. doi:10.1016/0039-9140(64)80128-4

He S, Zeng J, Habte BT, Jiang FM (2016) Numerical reconstruction of microstructure of graphite anode of lithium-ion battery. Sci Bull 61:656–664. doi:10.1007/s11434-016-1048-4

Huang G, Chen T, Chen W, Wang Z, Chang K, Ma L, Lee JY (2013) Graphene-like MoS_2/graphene composites: cationic surfactant-assisted hydrothermal synthesis and electrochemical reversible storage of lithium. Small 9:3693–3703. doi:10.1002/smll.201300415

Huang ZX, Wang Y, Zhu YG, Shi Y, Wong JI, Yang HY (2014) 3D graphene supported MoO_2 for high-performance binder-free lithium ion battery. Nanoscale 6:9839–9845. doi:10.1039/C4NR01744G

Janssen AH, Schmidt I, Jacobsen CJH, Koster AJ, De Jong KP (2003) Exploratory study of mesopore templating with carbon during zeolite synthesis. Micropor Mesopor Mat 65:59–75. doi:10.1016/j.micromeso.2003.07.003

Ji L, Lin Z, Alcoutlabi M, Zhang X (2011) Recent developments in nanostructured anode materials for rechargeable lithium-ion batteries. Energy Environ Sci 4:2682–2699. doi:10.1039/C0EE00699H

Jiang F, Yang LW, Tian Y, Yang P, Hu SW, Huang K, Wei XL, Zhong JX (2014) Bi-component MnO/ZnO hollow microspheres embedded in reduced graphene oxide as electrode materials for enhanced lithium storage. Ceram Int 40:4297–4304. doi:10.1016/j.ceramint.2013.08.094

Ku JH, Jung YS, Lee KT, Kim CH, Oh SM (2009) Thermoelectrochemically activated MoO_2 powder electrode for lithium secondary batteries. J Electrochem Soc 156: A688–A693. doi:10.1149/1.3141670

Liu BY, Fan CH, Chen JW, Wang JH, Lu ZP, Ren JY et al (2016) Low temperature in situ synthesis and the formation mechanism of various carbon-encapsulated nanocrystals by the electrophilic oxidation of metallocene complexes. Nanotechnology 27: 075603. doi:10.1088/0957-4484/27/7/075603

Liu BY, Fan CH, Chen JW, Zhou Y, Dong LH, Wang JH (2015b) Low temperature one-step synthesis of carbon co-encapsulated NiS_2, NiS and S_8 nanocrystals by electrophilic oxidation of nickelocene. Mater Lett 142:90–93. doi:10.1016/j.matlet.2014.11.147

Liu BY, Huang HP, Zhang FH, Zhou Y, Li WG, Zhang JW (2012a) Agglomerates of amorphous carbon nanoparticles synthesized by a solution-phase method. Mater Lett 66: 199–202. doi:10.1016/j.matlet.2011.08.111

Liu X, Ji W, Liang J, Peng L, Hou W (2014b) MoO_2@carbon hollow microspheres with tunable interiors and improved lithium-ion battery anode properties. Phys Chem Chem Phys 16:20570–20577. doi:10.1039/C4CP02960G

Liu BY, Jia DC, Zhou Y, Feng HB, Meng QC (2007) Low temperature synthesis of amorphous carbon nanotubes in air. Carbon 45:1710–1713. doi:10.1016/j.carbon.2007.04.014

Liu H, Su D, Zhou R, Sun B, Wang G, Qiao SZ (2012b) Highly ordered mesoporous MoS_2 with expanded spacing of the (002) crystal plane for ultrafast lithium ion storage. Adv Energy Mater 2:970–975. doi:10.1002/aenm.201200087

Liu BY, Zhang FH, Wu QL, Wang JH, Li WG, Dong LH et al (2015a) Low temperature synthesis of carbon encapsulated Fe_7S_8 nanocrystals as high-performance anode for lithium-ion batteries. Mater Chem Phys 151:60–65. doi:10.1016/j.matchemphys.2014.11.033

Liu B, Zhao X, Tian Y, Zhao D, Hu C, Cao M (2013) A simple reduction process to synthesize MoO_2/C composites with cage-like structure for high-performance lithium-ion batteries. Phys Chem Chem Phys 15:8831–8837. doi:10.1039/C3CP44707C

Liu BY, Zhong N, Fan CH, Zhou Y, Fan YH, Yu SQ et al (2014a) Low temperature synthesis and formation mechanism of carbon encapsulated nanocrystals by electrophilic oxidation of ferrocene. Carbon 68:573–582. doi:10.1016/j.carbon.2013.11.037

Mancini M, Nobili F, Tossici R, Wohlfahrt-Mehrens M, Marassi R (2011) High-performance, environmentally friendly and low cost anodes for lithium-ion battery based on TiO_2 anatase and water soluble binder carboxymethyl cellulose. J Power Sources 196:9665–9671. doi:10.1016/j.jpowsour.2011.07.028

Sasaki T, Ukyo Y, Novák P (2013) Memory effect in a lithium-ion battery. Nat Mater 12:569–575. doi:10.1038/nmat3623

Sen UK, Mitra S (2013) High-rate and high-energy-density lithium-ion battery anode containing 2D MoS_2 nanowall and cellulose binder. ACS Appl Mater Inter 5:1240–1247. doi:10.1021/am3022015

Shi Y, Guo B, Corr SA, Shi Q, Hu YS, Heier KR et al (2009) Ordered mesoporous metallic MoO_2 materials with highly reversible lithium storage capacity. Nano Lett 9:4215–4220. doi:10.1021/nl902423a

Sun Y, Hu X, Jimmy CY, Li Q, Luo W, Yuan L et al (2011) Morphosynthesis of a hierarchical MoO_2 nanoarchitecture as a binder-free anode for lithium-ion batteries. Energ Environ Sci 4:2870–2877. doi:10.1039/C1EE01189H

Wang Z, Chen JS, Zhu T, Madhavi S, Lou XW (2010) One-pot synthesis of uniform carbon-coated MoO_2 nanospheres for high-rate reversible lithium storage. Chem Commun 46: 6906–6908. doi:10.1039/C0CC01174F

Wang X, Xiao Y, Wang J, Varadaraju UV (2015) Facile fabrication of molybdenum dioxide/nitrogen-doped graphene hybrid as high-performance anode material for lithium ion batteries. J Power Sources 274:142–148. doi:10.1016/j.jpowsour.2014.10.031

Xu Y, Yi R, Yuan B, Wu X, Dunwell M, Lin Q et al (2012) High capacity MoO_2/graphite oxide composite anode for lithium-ion batteries. J Phys Chem Lett 3:309–314. doi:10.1021/jz201619r

Yang L, Liu L, Zhu Y, Wang X, Wu Y (2012) Preparation of carbon coated MoO_2 nanobelts and their high-performance as anode materials for lithium ion batteries. J Mater Chem 22: 13148–13152. doi:10.1039/C2JM31364B

Zhang HJ, Wang KX, Wu XY, Jiang YM, Zhai YB, Wang C et al (2014) MoO_2/Mo_2C heteronanotubes function as high-performance Li-ion battery electrode. Adv Funct Mater 24: 3399–3404. doi:10.1002/adfm.201303856

Zhang J, Yu A (2015) Nanostructured transition metal oxides as advanced anodes for lithium-ion batteries. Sci Bull 60:823–838. doi:10.1007/s11434-015-0771-6

Zhou L, Wu HB, Wang Z, Lou XW (2011) Interconnected MoO_2 nanocrystals with carbon nanocoating as high-capacity anode materials for lithium-ion batteries. ACS Appl Mater Inter 3: 4853–4857. doi:10.1021/am201351z

Zhou X, Yin YX, Wan LJ, Guo YG (2012) Self-assembled nanocomposite of silicon nanoparticles encapsulated in graphene through electrostatic attraction for lithium-ion batteries. Adv Energy Mater 2:1086–1090. doi:10.1002/aenm.201200158